Supplementary Information for

Deep-subwavelength exceptional point in microwave plasmonic resonators for enhanced sensing

Tian Shuo Bai[1,2], Xuanru Zhang[1,2]*, Wan Zhu Wang[1,2], Jingjing Zhang[1,2], and Tie Jun Cui[1,2]*

[1]State Key Laboratory of Millimeter Waves, Southeast University, Nanjing 210096, China

[2]School of Information Science and Engineering, Southeast University, Nanjing 210096, China

*Corresponding authors: zhangxru@seu.edu.cn, tjcui@seu.edu.cn

Table of contents

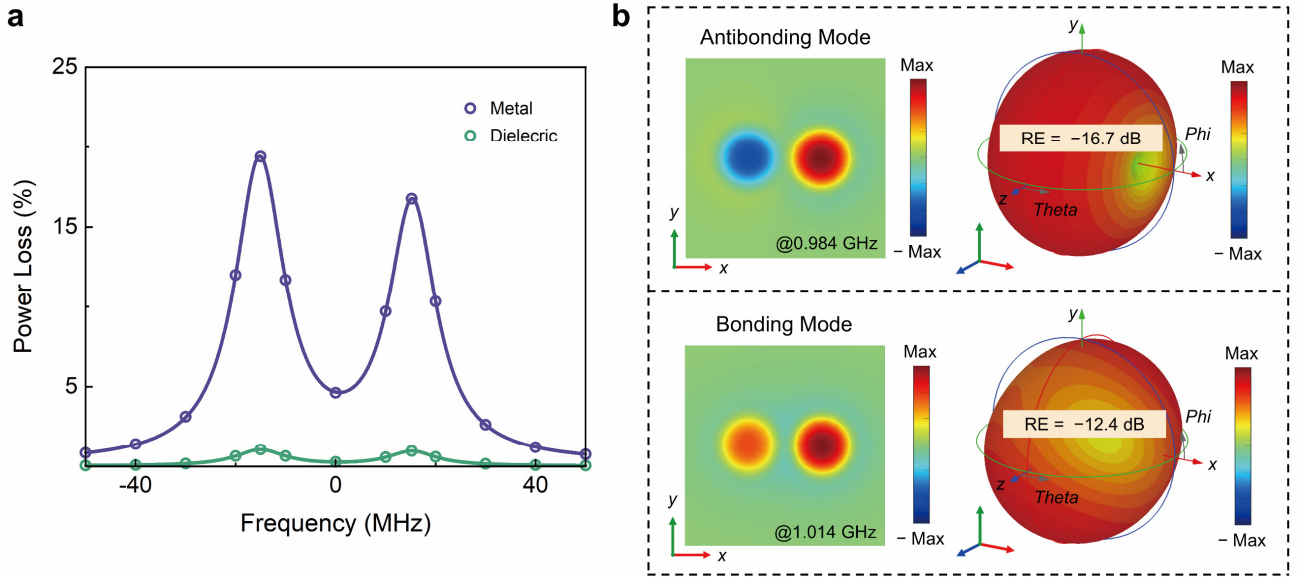**Supplementary Note 1. Loss Mechanism Analysis of the Antibonding and Bonding Modes**

The damping rate γ_a (γ_b) of the antibonding (bonding) mode is derived from the intrinsic loss and the escape loss from waveguide ports for the $\alpha = 0°$ case, where there is no intermodal coupling:

$$\begin{cases} \gamma_a = \dfrac{1}{\tau_{0a}} + \dfrac{1}{\tau_{1a}} + \dfrac{1}{\tau_{2a}} \\ \gamma_b = \dfrac{1}{\tau_{0b}} + \dfrac{1}{\tau_{1b}} + \dfrac{1}{\tau_{2b}} \end{cases} \tag{1}$$
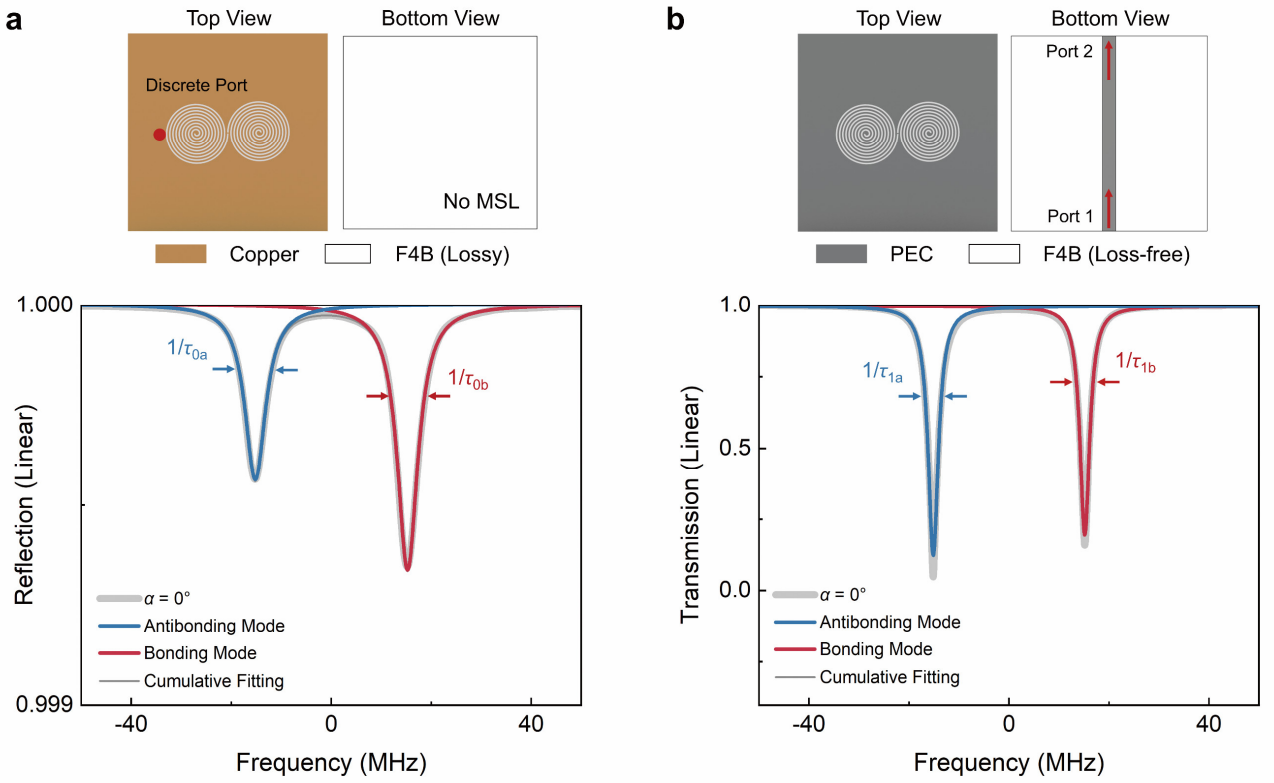
Here, $1/\tau_{0a}$ ($1/\tau_{0b}$) represents the intrinsic loss of the antibonding (bonding) mode. $1/\tau_{1a}$ ($1/\tau_{1b}$) and $1/\tau_{2a}$ ($1/\tau_{2b}$) represent the escape loss of the antibonding (bonding) mode from waveguide ports 1 and 2 respectively. We remark that the intrinsic losses of the antibonding and bonding modes are equal ($1/\tau_{0a}$ = $1/\tau_{0b}$) due to the mutual balance between material absorption loss and radiation loss, as shown in Supplementary Fig. 1.

Supplementary Fig. 1 | Intrinsic loss analysis of the antibonding and bonding mode for $\alpha = 0°$ case. a, Material absorption loss from the metal (copper) and the substrate (F4B). **b,** Radiation loss emitted into free space.

Then, the multipeak fitting method in the manuscript is used to identify the aforementioned losses from the full width at half maximum (FWHM) of the reflection and transmission spectra under different simulation settings[8,9], as shown in Supplementary Fig. 2. The excitation via a single discrete port is weak enough to ensure minimal impact on the eigenmodes, making it suitable for analyzing the intrinsic losses of the antibonding mode and the bonding mode. The intrinsic decay rates of the

antibonding mode and the bonding mode feature $1/\tau_{0a} = 1/\tau_{0b}$, as shown in Supplementary Fig. 2a. The escape losses of the antibonding and bonding modes can be calculated in loss-free structure, assuming that their radiation losses are negligible due to the strong field confinement in deep-subwavelength resonance units[10]. The escape losses of the antibonding and bonding modes also feature $1/\tau_{1a} = 1/\tau_{1b}$, as shown in Supplementary Fig. 2b. In such a reciprocal two-port system, the escape losses of the mode to port 1 and port 2 can be considered identical, with the relationships $1/\tau_{1a} = 1/\tau_{2a}$ and $1/\tau_{1b} = 1/\tau_{2b}$. Hence, the above results indicate that the two split resonances feature approximately equal damping rates ($\gamma_a = \gamma_b$), as shown in Fig. 2e in the manuscript.

Supplementary Fig. 2 | Loss fitting process using the multipeak fitting method. a, Intrinsic loss $1/\tau_{0a}$ ($1/\tau_{0b}$) of the antibonding (bonding) mode for $\alpha = 0°$ case. **b,** Escape loss $1/\tau_{1a}$ ($1/\tau_{1b}$) of the antibonding (bonding) mode from the waveguide port 1.

Meanwhile, the damping rates γ_+ (γ_-) of the mode $+$ ($-$) can also be determined based on the loss fitting process described above before reaching the EP state ($\alpha > 0°$), where the intermodal coupling is present. The fitted values are shown in Supplementary Table 1.

Supplementary Table 1 | Fitting parameters of the theoretical TCMT model.

α	$\kappa_{ab} = \kappa_{ab}{}^*$	κ_{1a}	κ_{1b}	$1/\tau_{1a}$	$1/\tau_{1b}$
0°	0	1.28	1.16	1.52	1.58
15°	5.5i	1.50	1.43	1.90	2.00
30°	11i	1.98	2.03	2.80	2.80
39°	15i	2.41	2.46	5.00	5.00
45°	16i	2.28	2.60	6.00	6.80
55°	18i	2.28	2.51	9.00	10.40

Supplementary Note 2. Coupling Mechanism Between the Antibonding and Bonding Modes

The coupling mechanism is elucidated by analyzing the overlap integral of the wave functions[11,12]. The wave functions of the SLSP mode supported by the resonance unit on the left (right) is ψ_L (ψ_R). The strong evanescent field coupling between two resonance units can be described by:

$$\begin{cases} \kappa_{LR} \propto I_{LR} = \int \psi_L{}^* \psi_R dV = \mathrm{Re}(I_{LR}) + i\,\mathrm{Im}(I_{LR}) \\ \kappa_{RL} \propto I_{RL} = \int \psi_R{}^* \psi_L dV = \mathrm{Re}(I_{LR}) - i\,\mathrm{Im}(I_{LR}) \end{cases} \quad (2)$$

where the real part of the overlap integral is much larger than the imaginary part ($\mathrm{Re}(I_{LR}) \gg \mathrm{Im}(I_{LR})$) and manifests as the coherent coupling. The imaginary part of the coupling coefficient can usually be ignored. Hence, the coupling coefficient features $\kappa_{LR} = \kappa_{LR} = \kappa$, where κ is a purely real number. The linear combinations between the two wave functions manifest as the antibonding and bonding modes. The wave functions of the antibonding mode (Ψ_a) and the bonding mode (Ψ_b) are given by:

$$\begin{cases} \Psi_a = C_1(\psi_L + \psi_R) \\ \Psi_b = C_2(\psi_L - \psi_R) \end{cases} \quad (3)$$

where C_1 (C_2) represents the normalization coefficients. The plus sign signifies that the two wave functions are in phase, whereas the minus sign indicates that they are in reverse phase. The above wave function satisfies the following normalization conditions of energy eigenstates:

$$\begin{cases} \int |\psi_L|^2 dV = 1 \\ \int |\psi_R|^2 dV = 1 \\ \int |\Psi_a|^2 dV = 1 \\ \int |\Psi_b|^2 dV = 1 \end{cases} \tag{4}$$

The third and fourth equations in equation (4) are expanded as:

$$\begin{cases} \int |\Psi_a|^2 dV = \int |C_1|^2 |\psi_L - \psi_R|^2 dV = |C_1|^2 \left(\int |\psi_L|^2 dV + \int |\psi_R|^2 dV - 2\operatorname{Re}(I_{LR}) \right) = 1 \\ \int |\Psi_b|^2 dV = \int |C_2|^2 |\psi_L + \psi_R|^2 dV = |C_2|^2 \left(\int |\psi_L|^2 dV + \int |\psi_R|^2 dV + 2\operatorname{Re}(I_{LR}) \right) = 1 \end{cases} \tag{5}$$

The normalization coefficient C_1 (C_2) is determined from equation (5). For the $\alpha = 0°$ case, the coupling coefficient κ_{ab} (κ_{ba}) is elucidated as the overlap integral of the wave functions between the antibonding mode and the bonding mode:

$$\begin{aligned} \kappa_{ab} &\propto \int \Psi_a^* \Psi_b dV = C_1 C_2 \int (\psi_L^* - \psi_R^*)(\psi_L + \psi_R) dV \\ &= i2 C_1 C_2 \operatorname{Im}(I_{LR}) \approx 0 \\ \kappa_{ba} &\propto \int \Psi_b^* \Psi_a dV = C_1 C_2 \int (\psi_L^* + \psi_R^*)(\psi_L - \psi_R) dV \\ &= -i2 C_1 C_2 \operatorname{Im}(I_{LR}) \approx 0 \end{aligned} \tag{6}$$

Eq. (6) demonstrates the absence of the coupling for the $\alpha = 0°$ case, as $\operatorname{Im}(I_{LR})$ approaches zero.

When the rotation angle $\alpha \neq 0°$, the asymmetric excitation can facilitate the generation of the phase variation $\Delta\varphi$ in the wave functions of the two SLSP modes. Hence, the equation (3) is modified to:

$$\begin{cases} \Psi_a = C_1(\psi_L e^{-i\Delta\varphi} - \psi_R e^{i\Delta\varphi}) \\ \Psi_b = C_2(\psi_L e^{-i\Delta\varphi} + \psi_R e^{i\Delta\varphi}) \end{cases} \tag{7}$$

Here, $i\Delta\varphi$ presents phase advance, while $-i\Delta\varphi$ represents phase delay relative to the situation where $\alpha = 0°$. Similarly, the overlap integral between the wave functions of the two SLSP modes is given by:

$$\begin{cases} \tilde{I}_{LR} = \int \psi_L^* e^{i\Delta\varphi} \psi_R e^{i\Delta\varphi} dV = e^{i2\Delta\varphi} I_{LR} \\ \tilde{I}_{LR} = \int \psi_R e^{-i\Delta\varphi} \psi_L e^{-i\Delta\varphi} dV = e^{-i2\Delta\varphi} I_{RL} \end{cases} \tag{8}$$

Notice that the integrals in equation (8) satisfy conjugate symmetry ($\tilde{I}_{LR} = \tilde{I}_{RL}^*$), which derives from the phase variation $\Delta\varphi$ induced by asymmetric excitation. Hence, the coupling coefficient κ_{ab} (κ_{ba}) is modified to:

$$\kappa_{ab} \propto \int \Psi_a^* \Psi_b dV$$

$$= C_1 C_2 \int (\psi_L^* e^{i\Delta\varphi} - \psi_R^* e^{-i\Delta\varphi})(\psi_L e^{-i\Delta\varphi} + \psi_R e^{i\Delta\varphi})dV$$

$$= C_1 C_2 \left(\int |\psi_L|^2 dV - \int |\psi_R|^2 dV + \tilde{I}_{LR} - \tilde{I}_{RL} \right) \qquad (9)$$

$$= i C_1 C_2 \left(2\sin(2\Delta\varphi)\,\mathrm{Re}(I_{LR}) + 2\cos(2\Delta\varphi)\,\mathrm{Im}(I_{LR}) \right)$$

$$\approx 2 C_1 C_2 \kappa \sin(2\Delta\varphi) i$$

$$\kappa_{ba} \propto \int \Psi_b^* \Psi_a dV$$

$$= C_1 C_2 \int (\psi_L^* e^{i\Delta\varphi} + \psi_R^* e^{-i\Delta\varphi})(\psi_L e^{-i\Delta\varphi} - \psi_R e^{i\Delta\varphi})dV$$

$$= C_1 C_2 \left(\int |\psi_L|^2 dV - \int |\psi_R|^2 dV + \tilde{I}_{LR} - \tilde{I}_{RL} \right) \qquad (10)$$

$$= -i C_1 C_2 \left(2\sin(2\Delta\varphi)\,\mathrm{Re}(I_{LR}) + 2\cos(2\Delta\varphi)\,\mathrm{Im}(I_{LR}) \right)$$

$$\approx -2 C_1 C_2 \kappa \sin(2\Delta\varphi) i$$

Equations (9) and (10) theoretically elucidate that the coupling coefficients κ_{ab} and κ_{ba} are complex conjugates of each other ($\kappa_{ab} = \kappa_{ba}^*$) and exhibit dissipative coupling characterized by purely imaginary coupling. The phase variation $\Delta\varphi$ induced by asymmetric excitation can be utilized to adjust the coupling strength between Ψ_a and Ψ_b, following the relation $|\kappa_{ab}| \propto \Delta\varphi \propto \alpha$.

Supplementary Note 3. Theoretical Model Based on Temporal Coupled-Mode Theory

The coupled SLSP system can be modeled using the temporal coupled-mode theory (TCMT) to analyze the coupling between the antibonding and bonding modes. According to the TCMT, the dynamic equations of the antibonding mode (*a*) and the bonding mode (*b*) are given by:

$$\begin{cases} \dfrac{da}{dt} = i(\omega_a + i\gamma_a)a - \kappa_{ab}b + \kappa_{1a}s_{1+} \\[2mm] \dfrac{db}{dt} = i(\omega_b + i\gamma_b)b - \kappa_{ba}a + \kappa_{1b}s_{1+} \end{cases} \qquad (11)$$

The microstrip line on the backside carries a sinusoidal incoming wave s_{1+} towards the coupled SLSP system. Port 2 remains without excitation. The coefficient κ_{1a} (κ_{1b}) quantifies the degree of coupling between the antibonding (bonding) mode and the excitation s_{1+}. The coupling coefficient κ_{ab} (κ_{ba}) quantifies the coupling strength between the antibonding and bonding modes. The TCMT equations take the form:

$$i\begin{pmatrix} \omega A \\ \omega B \end{pmatrix} = i\begin{pmatrix} \omega_a + i\gamma_a & i\kappa_{ab} \\ i\kappa_{ba} & \omega_b + i\gamma_b \end{pmatrix}\begin{pmatrix} A \\ B \end{pmatrix} + \begin{pmatrix} \kappa_{1a}S_{1+} \\ \kappa_{1b}S_{1+} \end{pmatrix} = i\hat{H}\begin{pmatrix} A \\ B \end{pmatrix} + \begin{pmatrix} \kappa_{1a}S_{1+} \\ \kappa_{1b}S_{1+} \end{pmatrix} \tag{12}$$

After substituting $a = Ae^{i\omega t}$, $\dfrac{da}{dt} = \dfrac{dA}{dt}e^{i\omega t} + i\omega Ae^{i\omega t}$ (same for the bonding mode b and the sinusoidal incoming wave mode s_{1+}) and $\dfrac{dA}{dt} = 0$, $\dfrac{dB}{dt} = 0$ in a steady state. Here, $\hat{H}$ represents the non-Hermitian Hamiltonian. Equation (12) is sorted into:

$$\begin{pmatrix} i\Delta\omega_a + \gamma_a & \kappa_{ab} \\ \kappa_{ba} & i\Delta\omega_b + \gamma_b \end{pmatrix}\begin{pmatrix} A \\ B \end{pmatrix} = \begin{pmatrix} \kappa_{1a}S_{1+} \\ \kappa_{1b}S_{1+} \end{pmatrix} \tag{13}$$

where $\Delta\omega_a = (\omega - \omega_a)$ and $\Delta\omega_b = (\omega - \omega_b)$. Then, solving Equation (13) yields the amplitudes A and B in the following forms:

$$\begin{pmatrix} A \\ B \end{pmatrix} = \begin{pmatrix} i\Delta\omega_a + \gamma_a & \kappa_{ab} \\ \kappa_{ba} & i\Delta\omega_b + \gamma_b \end{pmatrix}^{-1}\begin{pmatrix} \kappa_{1a}S_{1+} \\ \kappa_{1b}S_{1+} \end{pmatrix} \tag{14}$$

According to the relationship of energy conservation, the incoming and outgoing ports satisfy the following relationship:

$$S_{2-} = S_{1+} - \kappa_{1a}A - \kappa_{1b}B \tag{15}$$

Hence, according to equations (14) and (15), the transmission coefficients can be presented in the form:

$$T = \frac{S_{2-}}{S_{1+}} = 1 - \frac{\kappa_{1a}A + \kappa_{1b}B}{S_{1+}} = 1 - \begin{pmatrix} \kappa_{1a} & \kappa_{1b} \end{pmatrix}\begin{pmatrix} i\Delta\omega_a + \gamma_a & \kappa_{ab} \\ \kappa_{ba} & i\Delta\omega_b + \gamma_b \end{pmatrix}^{-1}\begin{pmatrix} \kappa_{1a} \\ \kappa_{1b} \end{pmatrix} \tag{16}$$

The fitting results are shown in Fig. 3 in the manuscript. The fitting parameters of the theoretical TCMT model are illustrated in Supplementary Table 1.

Supplementary Note 4. Limitation of Solving the Intrinsic Hamiltonian Equation

The limitations of solving the intrinsic Hamiltonian are elucidated below. As shown in equation (12), the non-Hermitian Hamiltonian of the coupled-SLSP system can be obtained in the absence of external excitation S_{1+}:

$$\begin{pmatrix} \omega A \\ \omega B \end{pmatrix} = \begin{pmatrix} \omega_a + i\gamma_a & i\kappa_{ab} \\ i\kappa_{ba} & \omega_b + i\gamma_a \end{pmatrix}\begin{pmatrix} A \\ B \end{pmatrix} = \hat{H}\begin{pmatrix} A \\ B \end{pmatrix} \tag{17}$$

The Hamiltonian of the system can be decomposed into Hermitian and non-Hermitian terms:

$$\hat{H} = \begin{pmatrix} \omega_a + i\gamma_a & i\kappa_{ab} \\ i\kappa_{ba} & \omega_b + i\gamma_b \end{pmatrix}$$
$$= \begin{pmatrix} \omega_0 + i\gamma_0 & 0 \\ 0 & \omega_0 + i\gamma_0 \end{pmatrix} + \begin{pmatrix} \Delta\omega + i\Delta\gamma & i\kappa_{ab} \\ i\kappa_{ba} & -\Delta\omega - i\Delta\gamma \end{pmatrix} \qquad (18)$$
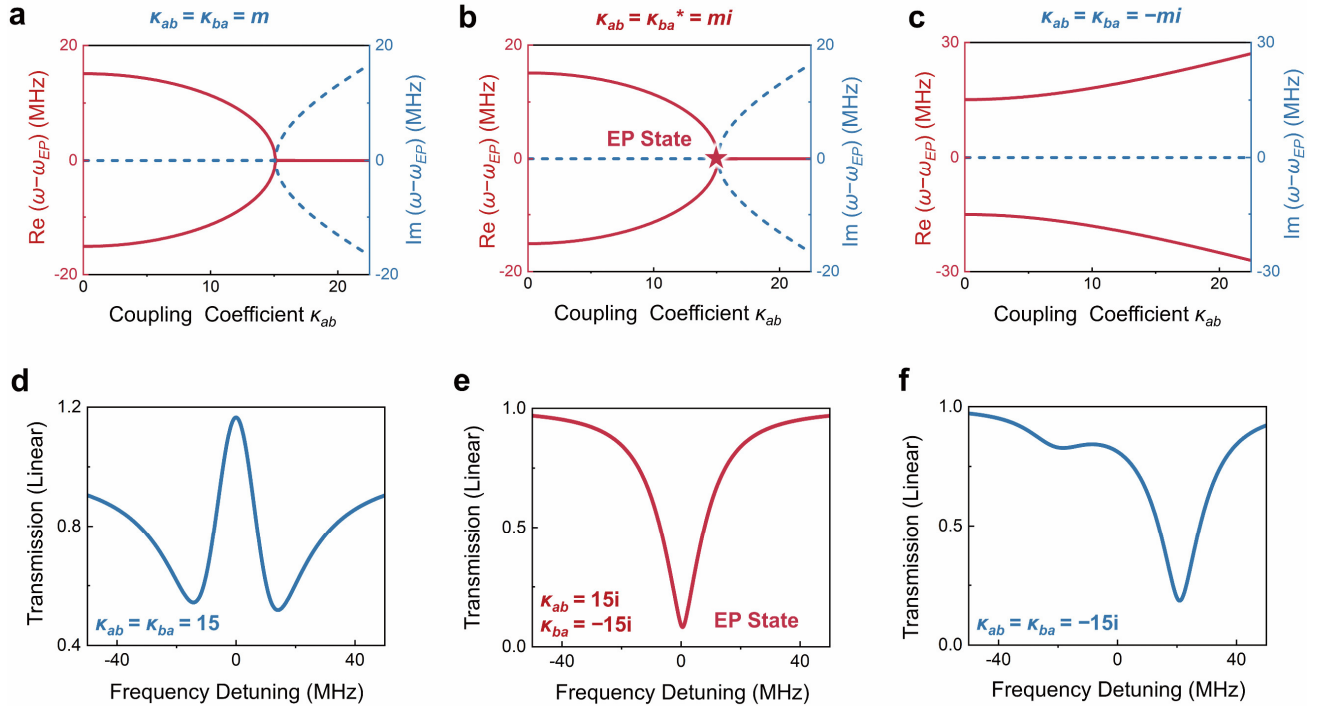
in which

$$\begin{cases} \omega_0 = \dfrac{\omega_a + \omega_b}{2}, & \gamma_0 = \dfrac{\gamma_a + \gamma_b}{2} \\ \Delta\omega = \dfrac{\omega_a - \omega_b}{2}, & \Delta\gamma = \dfrac{\gamma_a - \gamma_b}{2} \end{cases} \qquad (19)$$

The eigenfrequencies $\omega_\pm$ in this non-Hermitian system follow:

$$\omega_\pm = \omega_0 + i\gamma_0 \pm \sqrt{(\Delta\omega + i\Delta\gamma)^2 - \kappa_{ab}\kappa_{ba}} \qquad (20)$$

$\Delta\gamma$ is approximately zero as demonstrated in Supplementary Note I. Hence, the EP state can be achieved as the square root term approaches zero, which can occur with different values of the coupling coefficients, i.e., through various coupling mechanisms.

Supplementary Fig. 3 | The eigenfrequencies and transmission spectra are calculated using the TCMT model for three different combinations of κ_{ab} and κ_{ba}.

The TCMT equations are solved with different combinations of κ_{ab} and κ_{ba}, which can all lead to a degenerate eigenfrequency in equation (20) but present different transmission curves as shown in Supplementary Fig. 3. For the case $\kappa_{ab} = \kappa_{ab} = m$ (m is a purely real number), the EP state occurs in the eigenfrequencies derived from the Hamiltonian, while the transmission spectrum does not, as shown in Supplementary Figs. 3a and d. The EP state occurs in the eigenfrequencies and the transmission spectrum only when $\kappa_{ab} = \kappa_{ba}^* = mi$, as shown in Supplementary Figs. 3b and e. Both the eigenfrequencies and the transmission spectrum always exhibit a split resonance for the case $\kappa_{ab} = \kappa_{ba} = -mi$, as shown in Supplementary Figs. 3c and f.

Supplementary Note 5. Self-Made Near-Field Mapping System for Verifying the Fabricated EP Sensor

A self-made near-field mapping system is used to measure the $|E_z|$ fields for verifying the fabricated EP state, as shown in Fig. 5a of the manuscript. The sensor's input and output ports are equipped with SMA connectors for exciting the EP state. The self-made near-field mapping system is composed of a scanner loaded with a near-field probe, displacement control system, and vector network analyzer (VNA). The input port of the vector network analyzer feeds energy into the EP sensor through the coaxial cable and one SMA connector, while the other SMA connector is connected to a 50 Ω matched load. The near-field probe is a vertical electric monopole, which was made by exposing the center conductor out of a coaxial cable. The near-field probe is positioned 4 mm away from the surface of the sensor.

Then, the $|E_z|$ fields of the fabricated EP state at resonance frequencies were measured using the aforementioned self-made near-field mapping system. It can be observed that the electric field of one of the resonators is completely suppressed, while the electric field is localized in the other resonator. This is consistent with the simulated results shown in Fig. 5d of the manuscript and confirms that the fabricated sample is located indeed at the EP state.

References

1. Peng, B. et al. Chiral modes and directional lasing at exceptional points. *Proc. Natl. Acad. Sci. U. S. A.* **113**, 6845-6850 (2016).

2. Hokmabadi, M. P., Schumer, A., Christodoulides, D. N. & Khajavikhan, M. Non-Hermitian ring laser gyroscopes with enhanced Sagnac sensitivity. *Nature* **576**, 70-74 (2019).

3. Chen, J. M. et al. Coherent-Resonance Enhancement of Sensing at the Exceptional Points. *Adv. Opt. Mater.* **12**, 202302268 (2024).

4. Liao, Z. et al. Microwave Plasmonic Exceptional Points for Enhanced Sensing. *Laser Photonics Rev.* **17**, 202300276 (2023).

5. Bai, T. S., Wang, W. Z., Zhang, X. R. & Cui, T. J. Exceptional Point in a Microwave Plasmonic Dipole Resonator for Sub-Microliter Solution Sensing. *Adv. Funct. Mater.* **34**, 202312170 (2024).

6. Chen, W. J., Özdemir, S. K., Zhao, G. M., Wiersig, J. & Yang, L. Exceptional points enhance sensing in an optical microcavity. *Nature* **548**, 192-196 (2017).

7. Zhang, Y. R. et al. Reconfigurable exceptional point-based sensing with 0.001λ sensitivity using spoof localized surface plasmons. *Adv. Photon. Nexus* **3**, 056004 (2024).

8. Zhang, X. R. et al. Spoof Localized Surface Plasmons for Sensing Applications. *Adv. Mater. Technol.* **6**, 202000863 (2021).

9. Zhang, X. R., Yan, R. T. & Cui, T. J. High-FoM Resonance in Single Hybrid Plasmonic Resonator via Electromagnetic Modal Interference. *IEEE Trans. Antennas Propag.* **68**, 6447-6451 (2020).

10. Deng, Z. L., Shi, T., Krasnok, A., Li, X. P. & Alù, A. Observation of localized magnetic plasmon skyrmions. *Nat. Commun.* **13**, 8 (2022).

11. Lin, J. et al. Tailoring the lineshapes of coupled plasmonic systems based on a theory derived from first principles. *Light Sci. Appl.* **9**, 158 (2020).

12. Yang, Y. M. et al. Radiative anti-parity-time plasmonics. *Nat. Commun.* **13**, 7678 (2022).